nature communications

Article

https://doi.org/10.1038/s41467-025-64953-3

Mechanically steered photon upconversion and circularly polarized luminescence in stretchable photonic crystal films

Received: 21 May 2025

Accepted: 2 October 2025

Published online: 12 November 2025

Check for updates

Zhi-Wang Luo[1,2,3], Honghan Ji[3,4], Xue Jin[3,4], Jun Song[2], Zhen-Qiang Yu[1] ✉, Pengfei Duan[3,4] ✉ & Tonghan Zhao[5] ✉

Photon-upconverted circularly polarized luminescence (UC-CPL) based on triplet-triplet annihilation (TTA) holds considerable promise for innovative applications. However, existing strategies encounter difficulties in concurrently achieving tunable TTA photon upconversion (TTA-UC) performance and a high luminescence dissymmetry factor (g_{lum}) in the solid state. In this study, we design and fabricate flexible and stable upconverted stretchable photonic crystal (SPC) films. These films demonstrate dynamically tunable TTA-UC intensity and UC-CPL in response to mechanical stretching. Notably, while the TTA-UC intensity initially diminishes upon stretching the upconverted SPC film, it subsequently exhibits significant enhancement when the photonic bandgap edge aligns with the TTA-UC emission wavelength. Furthermore, stretching the upconverted SPC film can invert the circular polarization direction of the UC-CPL, with the g_{lum} value varying from +0.50 to −0.60. Consequently, these upconverted SPC films, characterized by their tunable structural color and adjustable UC-CPL, achieve visual flexible dynamic information display and encryption. This research offers promising perspectives for the development of advanced chiral UC-CPL materials and their potential applications in fields such as information encryption and flexible 3D displays.

Triplet-triplet annihilation-based photon upconversion (TTA-UC) facilitates the transformation of low-energy photons (long-wavelength light) into high-energy photons (short-wavelength light)[1–3]. This process initiates when a sensitizer absorbs long-wavelength light, transitioning to an excited singlet state, followed by an intersystem crossing to an excited triplet state. Subsequent triplet-triplet energy transfer (TTET) from the sensitizer populates the triplet state of an acceptor. The collision of two triplet acceptors then results in one acceptor returning to its ground state while the other is promoted to an excited singlet state via triplet-triplet annihilation. Finally, the excited singlet acceptor emits short-wavelength light[2,4–10]. Compared to rare-earth-doped upconversion materials, TTA-UC offers the advantages of operating at lower excitation power densities and involving simpler material preparation[7,11,12]. These attributes make TTA-UC highly promising for diverse applications, including optical and biological imaging, photovoltaic devices, anti-counterfeiting technology, and information encryption[13–23]. Most TTA-UC research has been conducted in deoxygenated solutions at room temperature, a condition

---

[1]College of Chemistry and Environmental Engineering, Shenzhen University, Shenzhen, Guangdong, PR China. [2]College of Physics and Optoelectronic Engineering, Shenzhen University, Shenzhen, Guangdong, PR China. [3]CAS Key Laboratory of Nanosystem and Hierarchical Fabrication, National Center for Nanoscience and Technology (NCNST), Beijing, PR China. [4]University of Chinese Academy of Sciences, Beijing, PR China. [5]Institute of Microstructure Technology, Karlsruhe Institute of Technology, Eggenstein-Leopoldshafen, Germany. ✉e-mail: zqyu@szu.edu.cn; duanpf@nanoctr.cn; tonghan.zhao@kit.edu

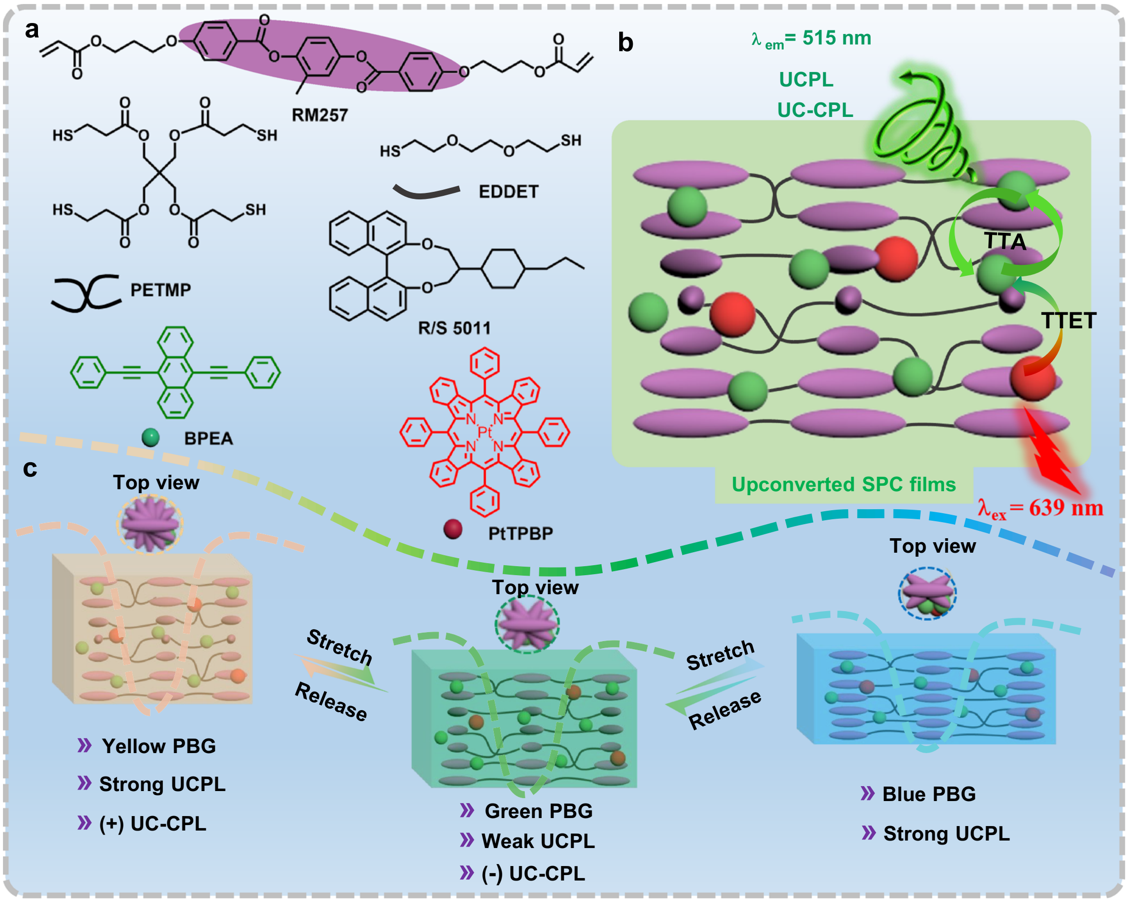

Fig. 1 | The composition and basic properties of upconverted stretchable photonic crystal (SPC) films. a Chemical structures of diacrylate mesogen (RM257), chiral dopants (R-/S-5011), cross-linker (PETMP), chain extender (EDDET), and the sensitizer (PtTPBP)/acceptor (BPEA) pair for fabricating upconverted SPC film. **b** Schematic diagram of the Triplet-triplet annihilation photon upconversion (TTA-UC) process including triplet-triplet energy transfer (TTET) from sensitizer to receptor and triplet-triplet annihilation (TTA) between two triplet acceptors for upconverted circularly polarized luminescence (UC-CPL) in the helical structure of the microscopic cross-linked network of upconverted SPC film. (λ_{ex} = 639 nm, λ_{em} = 515 nm) **c** Schematic illustration of reversable mechanically-steered photonic band gap (PBG), upconverted photoluminescence (UCPL), and UC-CPL.

that hinders the development of practical TTA-UC devices[22,24–26]. The incorporation of solid hosts represents an effective strategy to realize TTA-UC device fabrication, owing to the encapsulation and processability benefits[27–31]. For instance, Islangulov et al. reported green-to-blue upconverted photoluminescence (UCPL) in a rubbery polymer film utilizing palladium(II) octaethylporphyrin and 9,10-diphenylanthracene as the sensitizer and acceptor, respectively[32]. To date, various polymeric host matrices, such as polyurethane, polyethylene glycol, poly(methyl methacrylate), and cellulose acetate, have been successfully employed, advancing the field of solid-state TTA-UC[33–36]. Nevertheless, material deformation is often unavoidable in practical applications, and achieving external modulation of upconversion performance remains a significant challenge.

To investigate the influence of deformation on UCPL properties, a TTA-UC system comprising platinum(II) tetraphenyltetrabenzo porphyrin (PtTPBP) as the sensitizer and 9,10-bis(phenylethynyl) anthracene (BPEA) as the acceptor was incorporated into a stretchable liquid crystal elastomer (LCE) film. The reason for choosing the UC pair of BPEA and PtTPBP is that the red-light absorption capacity of PtTPBP enables UCPL with excitation of lower-energy light, the efficient emission characteristics of BPEA in the green light region, and the excellent triplet energy matching between the two[37,38]. However, a gradual decrease in TTA-UC intensity was observed during longitudinal stretching LCE film. To mitigate this challenge, stretchable photonic crystal (SPC) films—based on cholesteric liquid crystal elastomers—are identified as promising host materials. SPC films represent an emerging class of smart materials that combine the distinct chiral optical properties of a helical superstructure with the inherent flexibility and stability of elastomers[39–45]. Notably, the helical superstructure generates a photonic bandgap (PBG)[46–50], which can enhance luminescence at the band edge[51,52]. Concurrently, the stretchability of these elastomers enables the tuning of the PBG's band edge to align with the TTA-UC emission. This alignment is anticipated to counteract the deformation-induced decrease in emission intensity. Furthermore, the helically arranged structure of SPCs facilitates the generation of circularly polarized luminescence (CPL), characterized by the emission of left-handed and right-handed circularly polarized light with differing intensities[53–60]. Leveraging these unique features, the integration of SPCs as chiral templates with TTA-UC components is expected to enable the development of materials exhibiting both tunable TTA-UC and upconverted CPL (UC-CPL).

In this work, we fabricate the upconverted SPC films exhibiting mechanically manipulated TTA-UC efficiency and handedness of circular polarization. As illustrated in Fig. 1a, the TTA-UC pair, BPEA/PtTPBP, is integrated into SPC film. The elastomers are synthesized from the liquid crystal diacrylate monomer RM257, the chiral dopant R-/S-5011, the crosslinker pentaerythritol tetrakis(3-mercaptopropionate) (PETMP), and the chain extender 2,2′-(ethylenedioxy)diethanethiol (EDDET). Owing to the impermeability and inherent helicity of the SPC matrix, strong UC-CPL is observed under ambient conditions

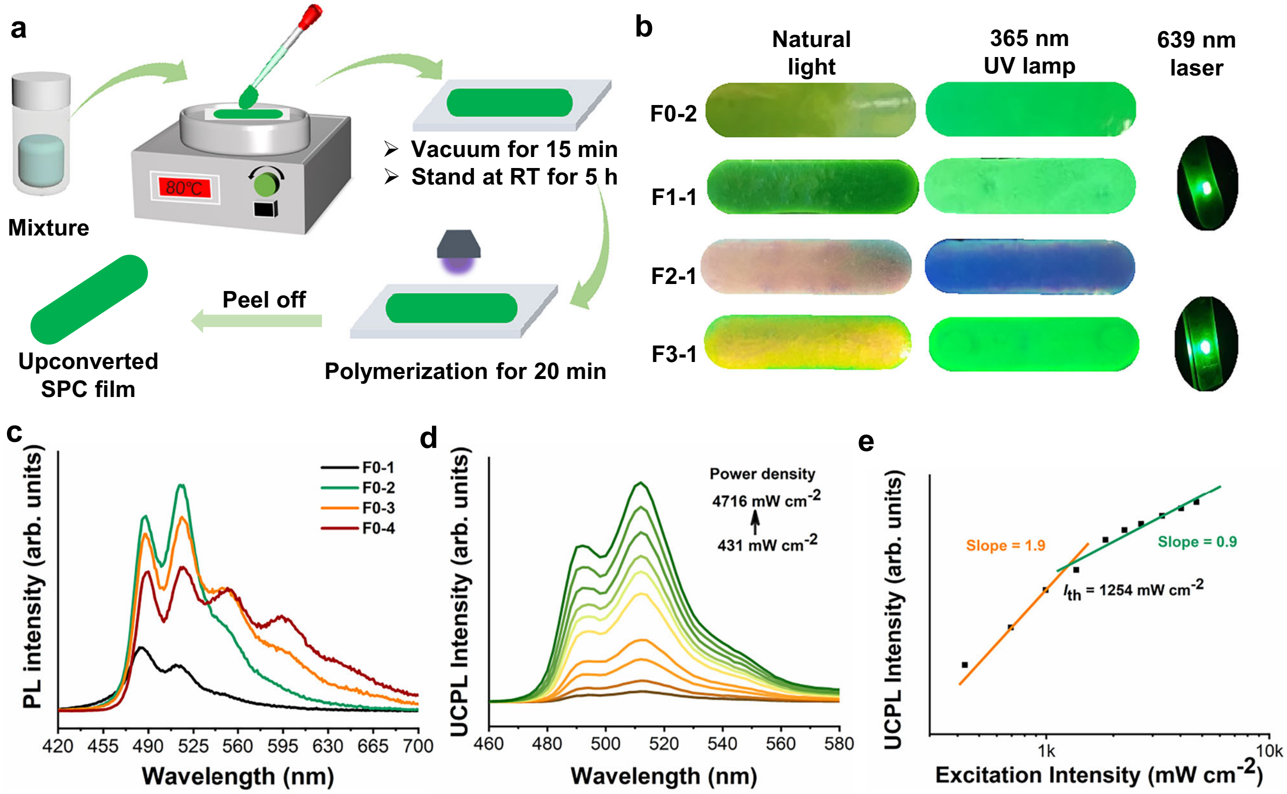

Fig. 2 | Preparation of thin films and UCPL. a Schematic illustration of fabricating process for upconverted SPC films via a facile anisotropic deswelling method that combined two-stage thiol-acrylate Michael addition and photopolymerization reactions. **b** The photos of films under natural light, 365 nm UV lamp, and 639 nm laser. **c** Fluorescence spectra of BPEA at different concentrations in liquid crystal elastomer (LCE) films. (λ_{ex} = 400 nm) **d** UCPL spectra of BPEA/PtTPBP (50:1) with different incident power density of 639 nm laser in LCE film; **e** Double-logarithmic plots of the UCPL intensity of BPEA/PtTPBP (50:1) as a function of excitation intensity of the 639 nm laser.

(Fig. 1b). Upon longitudinal stretching, the UCPL intensity initially decreased before subsequently increasing. More remarkably, the circular polarization direction of the UC-CPL inverted from left-handed to right-handed when the upconverted SPC film deformation reached 30%. Concurrently, the luminescence dissymmetry factor (g_{lum}) transitions from +0.50 to −0.60 (Fig. 1c). These dynamic control capabilities are attributed to the deformation-induced shift of the PBG position. Furthermore, we demonstrate the potential of these upconverted SPC films for advanced applications in mechanically tunable displays and multi-level information encryption, leveraging their modulated reflection colors, UCPL, and UC-CPL. The enhancement achieved in UCPL under high strain advances the fundamental understanding of the optical mechanisms of dynamic regulation, opening promising avenues for developing high-efficiency UCPL materials. Additionally, this work introduces a strategy for fabricating advanced chiral materials with UC-CPL properties, providing valuable insights for potential applications in information encryption and flexible 3D display technologies.

Results

Optimization of upconverted SPC films preparation and UCPL

We prepared the BPEA/PtTPBP-loaded upconverted SPC films by using a straightforward anisotropic swelling method combined with a two-stage thiol-acrylate addition and in-situ photopolymerization. The preparation process of the film and the appearance of some tested films are shown in Fig. 2a, b. For instance, LCEs with 0.5 wt% BPEA (F0-2), LCEs with BPEA/PtTPBP (F1-1), LCEs with S-5011 (F2-1), LCEs with S-5011 and BPEA/PtTPBP (F3-1). The green UCPL of F1-1 and F3-1 films is observed upon excitation of 639 nm laser in ambient air. While this wide agreement that oxygen can quench triplet excited state, this preparation process is conducive to removing oxygen from the film, such as vacuuming and polymerization. The Michael addition reaction and generated free radicals can react with active oxygen species during the polymerization process, leading to the formation of inactive peroxy radicals. This reaction effectively reduces the concentration of oxygen within the film, thereby creating an environment favorable for achieving TTA-UC[61–63].

To achieve optimal TTA-UC, we determined the ideal concentration of BPEA and the ratio of BPEA to PtTPBP through photoluminescence tests. The absorption and fluorescence spectra of BPEA and PtTPBP are shown in Supplementary Fig. 1. The concentration of the luminescent molecules plays a significant role in determining both the UCPL efficiency and spectrum in upconverted LCEs. At a low concentration, TTET from PtTPBP to BPEA is insufficient, while BPEA aggregates at an excessively high concentration, which paradoxically reduces luminescence efficiency. We prepared a series of achiral LCEs films containing varying mass fractions of BPEA at concentrations of 0.1 (F0-1), 0.5 (F0-2), 1.0 (F0-3), and 2.0 (F0-4) wt% and performed a comprehensive analysis of their optical performance (Supplementary Table 1). The fluorescence spectra indicate that the F0-1 exhibits distinct luminescence peaks at 488 and 515 nm (Fig. 2c). As the concentration of BPEA increases to 0.5 wt%, the luminescence peak at 488 nm weakens, while the peak at 515 nm increases due to self-absorption. As the concentration increases further in the films F0-3 and F0-4, distinct luminescence peaks appear at 556 nm and 596 nm, respectively. We speculate that this is due to the aggregation of BPEA molecules. We conducted verification through the color of the film and the texture under polarizing microscope (POM). The film turns yellow, and a clear red crystal is observed under POM (Supplementary Fig. 2). These results indicate the formation of aggregated states. Considering the impact of both luminescence efficiency and

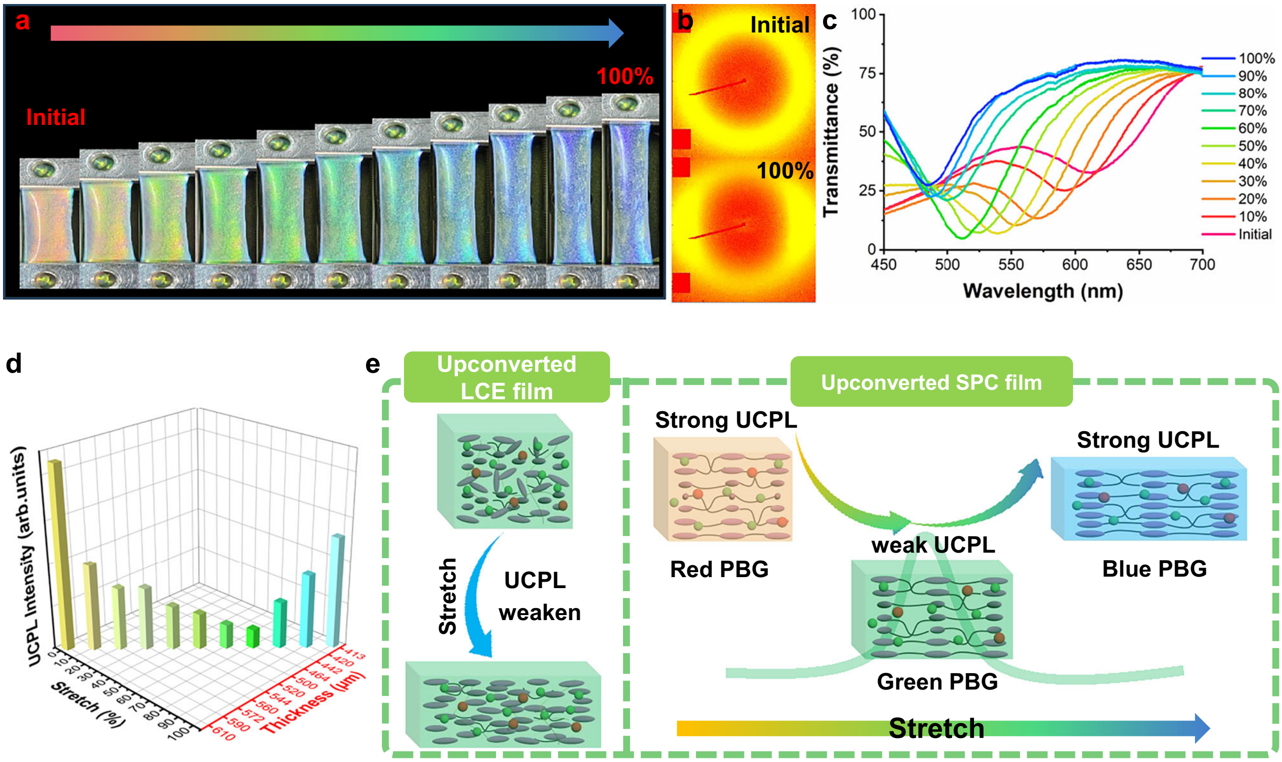

Fig. 3 | The basic properties of various films under dynamic stretching. **a** Photographs of a SPC film F2-1 being mechanically stretched. **b** The initial SPC film F2-1 corresponding wide-angle X-ray diffraction (WAXD) patterns of polydomain structure, and the 100% strained film corresponding WAXD patterns of monodomain structure. **c** Transmittance spectra of the initial F2-1 at various strains (from 0% to 100%) with no polarizer. **d** The relationship between different tensile lengths, thickness, and UCPL intensity of film F3-1. The original length of the above test films is 20 mm, and each stretch is 2 mm, a bar chart column represents a single measurement, $\lambda_{ex} = 639$ nm, $\lambda_{em} = 515$ nm. **e** Schematic diagram of tensile changes of thin films with and without PBG.

aggregation in the films, we determined the optimal concentration of BPEA is 0.5 wt%. As for the optimization of the PtTPBP content, we selected molar ratios of 50:1 (F1-1), 100:1 (F1-2), and 150:1 (F1-3) for the upconversion pair of BPEA/PtTPBP. The optical path for testing UCPL is shown in Supplementary Fig. 3, under irradiation with a 639 nm laser, remarkable UCPL signal is observed peaking at 515 nm (Fig. 2d and Supplementary Fig. 4a, c). The double-logarithmic plots of UCPL intensity as a function of excitation density exhibit the slope of fitted result transitioning from ~2 to ~1 (Fig. 2e and Supplementary Figs. 4b, d), confirming the TTA mechanism. In addition, the UCPL lifetime at 515 nm of F1-1, F1-2, and F1-3 is estimated to be 377, 295, and 339 μs, respectively, consistent with the long-lived triplet state annihilation mechanism (Supplementary Fig. 5). F1-1 shows a threshold excitation intensity of 1254 mW cm^{-2}, demonstrating it requires the lowest excitation intensity to achieve saturated upconversion efficiency among these three sets of samples. Therefore, we selected a BPEA concentration of 0.5 wt% in F1-1 and a molar ratio of BPEA to PtTPBP at 50:1 for the following investigation.

Dynamic regulation of UCPL in upconverted SPC films

To reveal the mechanical and optical properties of the prepared elastomer films under stretched operation, stress-strain and stretching-dependent UCPL tests were performed. We define the direction of the tensile force along the *x*-axis, the width of the film along the y-axis, and the thickness along the z-axis (Supplementary Fig. 6). The films F1-1, F2-1 and F3-1 exhibit excellent stress-strain characteristics at room temperature, with an elongation exceeding 100%, laying a foundation for subsequent experiments (Supplementary Fig. 7). Subsequently, the UCPL of the films F1-1 under mechanical stress was examined (Supplementary Fig. 8). The UCPL intensity gradually decreases as the tensile strain along the x-axis increases, which reveals that the tensile deformation of the film is detrimental to the upconversion performance.

The continuous suppression of UCPL during stretching harms the practical applications of upconverted LCEs films. We thus introduced chiral molecule S-5011 into the elastomer to prepare SPC films possessing helical superstructure, with the aim of enhancing UCPL through the PBG edge. The edge of the PBG can enhance the coupling effect and the photonic density of states[51,52,64,65]. To confirm such a scenario, the changes in the PBG position of F2-1 were investigated during stretching. As shown in Fig. 3a, the F2-1 exhibits notable discoloration at different elongation states. The color of the film changed from red via green to blue with continuous mechanical stretching. The reason for the blue shift of F2-1 color is that the reduction of the film thickness along the z-axis leads to a decrease in helical pitch (Supplementary Fig. 9), resulting in the PBG position moving to a short wavelength. Remarkably, this entire stretch-and-release process is fully reversible, with no noticeable delay between mechanical relaxation and color recovery (Supplementary Fig. 10). To further elucidate the mechanochromic mechanism of the stretched F2-1, qualitative analysis was conducted using POM and wide-angle X-ray diffraction (WAXD) measurements. As shown in Supplementary Fig. 11a, in the initial state, when the film F2-1 is rotated by 45° and 90°, there is no obvious change in the POM texture. When the elongation is 100%, the POM images show periodic changes from the dark field to the bright field with the film F2-1 rotates at 45° intervals, indicating that the texture of F2-1 and the arrangement of liquid crystal units deform along the mechanical stretching direction. Furthermore, as the F2-1 stretches, the WAXD patterns change from a ring to a pair of arcs (Fig. 3b). By performing an azimuthal angle integration of WAXD, no obvious peak is observed in the initial film, while after stretching, diffraction peaks appeared near 0° (360°) and 180° (Supplementary Fig. 11b). These results indicate that the polydomain structure in the initial F2-1 transitions to a monodomain structure with the stretched modulation. To gain insights into the mechanochromic response of F2-1, transmittance spectra were recorded. The position of the transmittance peak continuously shifts from 610 to 482 nm during uniaxial stretching (Fig. 3c). We further incorporated right-handed circularly polarized filter (R-CPF) and left-handed circularly polarized filter (L-CPF) into the transmittance test for the uniaxial strain experiment (Supplementary Fig. 12). The initial F2-1 exhibits characteristic transmittance only when the R-CPF is applied. Interestingly, the film starts reflecting certain wavelength in the L-CPF channel when stretched uniaxially by more than 40%. This result indicates that the F2-1 gradually transitions from a polydomain helical structure to a monodomain stratified structure, approaching a 1D Bragg reflector state that reflects both left- and right-handed circularly polarized light. Consequently, the PBG does not disappear when the elongation is less than 100%, allowing us to fully utilize the PBG-edge enhancing effect to enhance TTA-based UCPL.

We studied the TTA-UC properties of upconverted SPC film F3-1 during the uniaxial tensile process. The stress-dependent UCPL spectra reveals that the UCPL intensity initially decreases and then increases during the F3-1 stretching process (Fig. 3d and Supplementary Fig. 13). The UCPL intensity decreases from the initial value until the elongation reaches 70%, when it reaches the minimum UCPL intensity. When the elongation exceeds 70%, the UCPL increases. We found that at this point of 70% elongation, the position of PBG is near 515 nm (Supplementary Fig. 14), which corresponds to the emission wavelength of UCPL. When the elongation exceeds 70%, the PBG shifts towards a short wavelength; correspondingly, the UCPL peak locates at the edge of the PBG, enabling the enhancement of emission intensity. Furthermore, we conducted a study on the lifetime and upconversion efficiency (Φ_{UC}) of F3-1 at different stretching length positions (Supplementary Fig. 15 and Supplementary Table 3). The UCPL lifetime increases from the initial 189 μs to 268 μs accompanied by a decrease in Φ_{UC} when stretched to 70%, and then drops to 164 μs when reaching the band edge at 100% elongation (while the Φ_{UC} increases). For F1-1 films without PBG, the UCPL lifetime tends to stabilize from the initial 159 μs after stretched by 70%, while the Φ_{UC} continues to decrease. These results clearly indicate that the variation of the photonic density of states near the PBG improves the UCPL intensity through the resonance mechanism, providing strong experimental evidence for the role of the PBG-edge enhancing effect in UCPL[51,52,64,65]. Regarding the difference in the variation trend of UCPL between F1-1 and F3-1 during the stretching process, the schematic diagram in Fig. 3e illustrates the influence of two elastomers on UCPL. In the F1-1, the UCPL decreases gradually throughout the stretching process. On the other hand, when helical superstructure is formed in F3-1, the increase in UCPL is that the PBG-edge enhancing effect during the stretching process. These results prove our hypothesis that the band-edge enhancement effect of upconverted SPC film can mitigate the loss of UCPL intensity caused by the tensile deformation of the film.

Dynamic regulation of UC-CPL in upconverted SPC films

Encouraging by the excellent regulating properties of the PBG, we further investigated the UC-CPL performance of the upconverted SPC film under mechanical force. In chiral liquid crystal-based photonic crystals, the emission of circularly polarized light possesses distinct selectivity[66,67]. For instance, the left-handed photonic crystals film can reflect left-circularly polarized light while allowing the transmittance of right-circularly polarized light (Supplementary Fig. 16). We tested the PBG of the F3-2 film by circular dichroism (CD) spectroscopy (Fig. 4a). The CD spectra of initial film show a PBG centering at ~545 nm, while it shifts to ~514 nm after stretching. These results suggest that the degree of overlap between the PBG and UCPL peaks of BPEA can be dynamically adjusted. We established an optical testing setup by turning the angles between the quarter-wave plate and polarizer to measure UC-CPL intensity (Supplementary Fig. 17). Using the formula $I_{UC\text{-}CPL} = I_L - I_R$, where the I_L and I_R denote the intensity of left-handed and right-handed circularly polarized light, respectively, data presented in Fig. 4b shows that the UC-CPL inverts from a positive to a negative signal with the stretching of upconverted SPC film, corresponding to a transition from left-handed to right-handed UC-CPL. Furthermore, by applying the g_{lum} calculation formula $g_{lum} = 2 \times (I_L - I_R)/(I_L + I_R)$, we obtained the spectra of g_{lum} versus wavelength shown in Fig. 4c. The g_{lum} corresponding to the emission peak of initial film is +0.50, while stretching of the film inverts it to −0.60, confirming that tuning the PBG effectively alters the circular polarity of the UC-CPL. The g_{lum} values of initial and stretched states remain almost unchanged under 5 times stretching-releasing cycles in the same test conditions (Fig. 4d), proving good fatigue resistance of the film. Furthermore, we investigated the structural evolution of upconverted SPC film during stretching process through POM and WAXD. When the F3-2 film is stretched to 30% elongation, it exhibits a change in its structural color upon being rotated to an angle of 45°, while its brightness remains nearly constant (Fig. 4e). As the film is rotated further to 90°, its color reverts to that observed at the initial 0° position. This optical behavior is analogous to that of the unstretched film, suggesting that the liquid crystal texture is not significantly altered by the 30% strain. Figure 4f shows a circular ring in the initial state. After stretching of the film, only slight changes on the orientation distribution are observed (Supplementary Fig. 18). These experimental results indicate that the structural change of the stretched film is not significant, thus the influence of the linear polarization effect during the stretching process on UC-CPL is negligible. Based on these observations, a mechanism of UC-CPL inversion is depicted in Fig. 4g. According to the Bragg reflection, the reflected wavelength (λ) can be calculated by the formula $\lambda = n_o{}^*P\ \sin(\theta)$, where P is the pitch of the helical structure, n_0 is the average refractive index of the material, and θ is the angle of the incident light[68]. Here we define the wavelengths of PBG in the initial and stretched states as λ_1 and λ_2, respectively, and the peak position of UCPL as λ_{em}. In the initial state, PBG is far from the UCPL wavelength ($\lambda_1 \neq \lambda_{em}$), thus BPEA/PtTPBP emits left-handed UC-CPL upon excitation. On the other hand, after stretching, the PBG shifts and coincides with the position of the emission wavelength ($\lambda_2 \approx \lambda_{em}$). The system reflects the left-handed light while transmitting the right-handed light, thus generating the right-handed UC-CPL.

The application of upconverted SPC films in information display and encryption

We explored the potential applications of upconverted SPC films in dynamic information encryption and decryption based on their mechanically tunable color and UC-CPL characteristics. Especially, inspired by the display and concealment of information manipulated by the self-regulation mechanism of butterfly wings, a motion that dynamically conceals (upon folding) and reveals (upon spreading) their inherent structural coloration (Fig. 5a), we designed a manipulable application for displaying and hiding information. Initially, a butterfly-shaped mold was created using a laser marking device, followed by the infusion of the F3-2 formulation and subsequent polymerization, resulting in upconverted SPC films with butterfly shape, which serves as a medium for information encoding (Fig. 5b). At this point, information changes under static conditions are displayed. Under natural light, the butterfly-shaped films display a yellow structural color (I). Upon irradiation with a 639 nm laser, bright green UCPL (II) is observed, accompanied by distinct bright-dark variations under the CPFs. Weak luminescence is observed through the R-CPF (III), while strong luminescence is observed through the L-CPF (IV), confirming the emission of left-handed UC-CPL. We further manipulated the butterfly membrane. The structural color transitions from yellow to green (I′). When excited by 639 nm light, the UCPL becomes weaker (II′) compared to state (II). However, the opposite phenomenon is

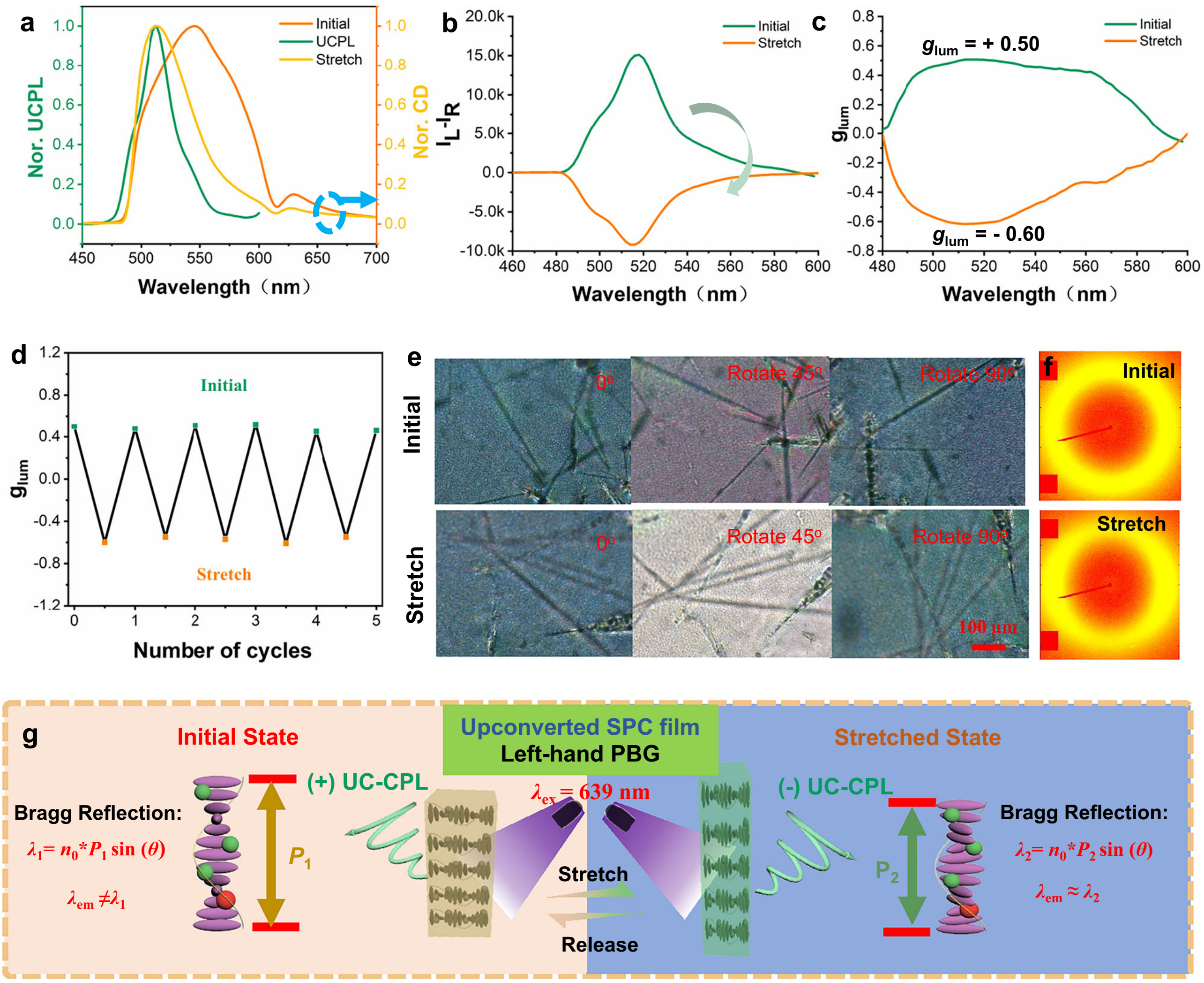

Fig. 4 | Dynamic regulation of UC-CPL. a The relationship between PBG and UCPL wavelengths under stretching of upconverted SPC film F3-2. The position of the luminescent peak is fixed, and PBG is dynamically adjusted with the stretching **b** UC-CPL spectra of initial and stretched film. The initial and stretched intensities are calculated according to the formula $I_{UC\text{-}CPL} = I_L - I_R$. **c** Distribution of luminescence dissymmetry factor (g_{lum}) values of initial and stretched film as a function of wavelength. The g_{lum} values are calculated from $g_{lum} = 2 \times (I_L - I_R)/(I_L + I_R)$. **d** Reversible changes of g_{lum} values (515 nm) against repeated stretching and releasing cycles of upconverted SPC film F3-2. **e** POM images of the upconverted SPC film F3-2 in transmission mode under crossed polarizers before and after being stretched (Scale bar = 100 μm). **f** The upconverted SPC film F3-2 corresponding WAXD in the initial state and stretched state. **g** Schematic diagram of dynamic regulation of UC-CPL by upconverted SPC film. The initial state is left-handed UC-CPL, and the state after stretching is right-handed UC-CPL.

observed through CPFs, with strong UC-CPL observed through the R-CPF (III′) and weak UC-CPL observed through the L-CPF (IV′). This demonstrates that these films not only enable structural color modulation through mechanical manipulation but also facilitate the regulation of UC-CPL, offering alternative insights into the dynamic applications of smart materials. Furthermore, the application of these materials in binary-encoded information encryption, utilizing both structural colors and UCPL, was investigated (Fig. 5c). In this scheme, the binary digit "0" is represented by the F-R-BPEA (F4-1) film, while "1" is encoded using the F-S-BPEA/PtTPBP (F3-2) film. These distinct films were integrated into a matrix to encode the binary message "CPL". Under ambient natural light, no discernible difference is apparent between the encoded regions. Similarly, while fluorescence is observable under 365 nm UV irradiation, the encrypted information remains concealed. However, the encoded message "CPL" can be revealed through specific decryption protocols. The primary decryption method involves observing changes in the structural color of the chiral photonic crystal films when viewed through a R-CPF. Under these conditions, bright areas indicate "1" and dark areas indicate "0". A secondary decryption pathway utilizes UCPL. Upon excitation at 639 nm, films containing the BPEA/PtTPBP TTA-UC components emit distinct UCPL spots, thereby allowing the retrieval of the "CPL" encoded information. This innovative approach leverages the unique optical characteristics of chiral photonic crystals and UCPL, presenting an alternative strategy for advanced information encryption.

Discussion

In summary, we fabricate upconverted SPC films that exhibit mechanically enhanced TTA-UC and tunable UC-CPL. Through mechanical stretching, the PBG edge of the upconverted SPC films can be precisely controlled to align with the UCPL wavelength, resulting in an enhanced UCPL intensity. Significantly, during this PBG shift, the UC-CPL signal inverts from positive to negative, with the corresponding g_{lum} value changing from +0.50 to −0.60. Inspired by biomimetic designs, these upconverted SPC films are successfully applied to achieve deformation-induced dynamic information display by modulating both structural color and UC-CPL through mechanical force. This study demonstrates the mechanical enhancement of TTA-

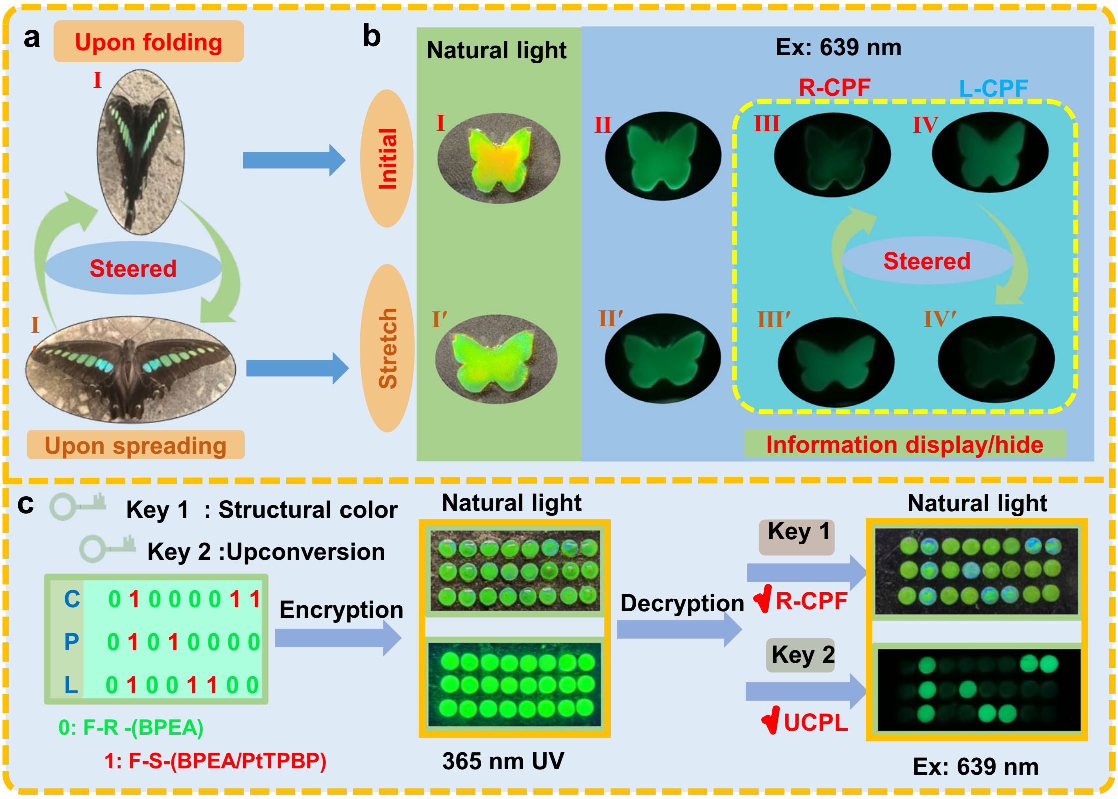

Fig. 5 | The applications of upconverted SPC films in dynamic information encryption and decryption. a In nature, butterflies display information by steering its wings manipulating their wings, dynamically conceals (I: upon folding) and reveals (I′: upon spreading) their inherent structural coloration. (Photo by the author). **b** Bionic patterning of upconverted SPC films inspired by butterflies (Butterfly wings upon folding correspond to the initial state of the film, and butterfly wings upon spreading correspond to the stretch state of the film, by artificially manipulating the film, different brightness and darkness UCPL can be exhibited at different circularly polarized filters); And group changes observed under different conditions. (I, I′ are photos taken in natural light, among them, I is in the initial state and I′ is in the stretched state; II, III, IV, II′, III′, IV′ are photos taken under 639 nm excitation and 580 nm short-pass filter, among them, II, III, IV are in the initial state and II′, III′, IV′ are in the stretched state). **c** The application of binary-encoded information encryption utilizing structural colors and UCPL.

UC and the achievement of tunable UC-CPL performance in the solid state. These findings provide potential insights into the development and application of advanced smart materials, particularly for dynamic displays and information encryption technologies.

Methods

Materials

The emitter 9,10-bis(phenylethynyl)anthracene (BPEA) was purchased from Shanghai Aladdin Biochemical Technology Co., LTD. Platinum(II) tetraphenyltetrabenzopor-phyrin (PtTPBP) (>95%) was purchased from Frontier Scientific, Inc. Liquid crystal crosslinking body 2-methyl-1,4-phenylenebis[4-(3-(acryloyloxy)propoxy)benzoate] (RM257) and photoinitiator 2,2-dimethoxy-2-phenylacetophenone (I-651, 99%) were purchased from Merck. The chiral dopant S (R) 5011 (>98%) was provided by Jiangsu Hecheng Display Technology Co., Ltd. Pentaerythritol tetrakis(3-mercaptopropionate) (PETMP), 2,2′-(Ethylenedioxy)diethanethiol (EDDET), and dipropylamine (DPA) were purchased from Shanghai Bidd Pharmaceutical Technology Co., LTD. The cleaned slide slot is 25 mm long, 1 mm wide, and 0.2 mm thick. The conventional reagents and solvents used were purchased from the public platform and the National Pharmaceutical Reagent Company and were not purified and used directly.

Characterizations

UV−Vis spectra were recorded in quartz cuvettes on a U-3900 spectrophotometer. Upconverted emission decays were recorded on a HORIBA Scientific Nanolog FL3-iHR320 spectrofluorometer using multichannel scaling. Fluorescence spectra were obtained using EDINBURGH FS5 Spectrofluorometer. Fluorescence lifetime measurements were recorded on the Edinburg FS5 fluorescence spectrometer using time-correlated single photon counting (TCSPC). Circular Dichroism (CD) spectra were recorded in films on a JASCO J-1500 spectrophotometer. Upconverting and downshifting photoluminescence and CPL measurements were performed on a monochromator equipped with a charge-coupled device detector (Andor Technology, iVac 316). A 639 nm continuous wave laser was chosen for excitation. The detection of CPL is set according to the description in Supplementary Fig. 16. Typically, the emissive light of samples passed through an achromatic broadband quarter-waveplate, which was used to separate the left (L, having intensity I_L) and right (R, having intensity I_R) circularly polarized components. The DS-/ UC-CPL signal was calculated as DS-/ UC-CPL = $I_L - I_R$. Polarizing optical microscopy (POM) was recorded on the Olympus X83 using a high-pressure mercury lamp as an excitation source for fluorescent images. Python Software Uses Spyder 5.4.3. XRD tests were performed using a Bruker D8 Discover diffractometer. WAXS and SAXS tests were performed using a Ganesha 300 XL SAXS system (SAXSLAB). A Shimadzu SES-1000 extensometer was employed to measure the elastic modulus, the failure strain, as well as the tensile strength of the networks with a constant extension rate of 1.0 mm/s at 25 °C.

Preparation of various films

The preparation method of the said film has similar values, and only the quality needs to be adjusted according to the Supplementary Table 1. Take the thin film F3-1 as an example: Weigh 150.00 mg RM257, 4.10 mg S5011, and place it in a 3 ml glass sheet. Add 70 μL of toluene, dissolve at 80 °C, and make it dissolve completely. Then let it cool at room temperature. Add 41.70 mg EDDET, 9.60 mg PETMP, and 2.00 mg I-651 in sequence and mix evenly. Finally, add Michael's added catalyst 1.00 mg DPA (in 50 μL toluene). The mixture was allowed to stand for ten minutes to initiate the Michael addition cross-linking reaction. Subsequently, tetrahydrofuran solution with sensitizer 0.054 mg PtTPBP and acceptor 1.02 mg BPEA was added, and pour into the mold on a heating plate at 80 °C to accelerate the evaporation of the solvent. The film was degassed under vacuum to promote the formation of a uniform structure, which is beneficial for the TTA-UC process. Finally, photopolymerization was performed to establish a stable cross-linked network structure.

Data availability

All data supporting this study, including detailed methods and experimental details, photophysical properties studies, are available in the Manuscript, Supplementary information, and Source Data file. Source data are provided with this paper.

References

1. Huang, L. et al. Triplet-triplet annihilation photon upconversion-mediated photochemical reactions. *Nat. Rev. Chem.* **8**, 238–255 (2024).
2. Li, J. K. et al. NIR–absorbing B,N–heteroarene as photosensitizer for high–performance NIR–to–blue triplet–triplet annihilation upconversion. *Angew. Chem. Int. Ed.* **62**, e202303093 (2023).
3. Monguzzi, A. et al. Low–power–photon up–conversion in dual–dye–loaded polymer nanoparticles. *Adv. Funct. Mater.* **22**, 139–143 (2011).
4. Han, J. et al. Amplification of circularly polarized luminescence through triplet–triplet annihilation-based photon upconversion. *J. Am. Chem. Soc.* **139**, 9783–9786 (2017).
5. Zhang, Q. et al. Crystalline hydrogen-bonded organic framework for air-tolerant triplet–triplet annihilation upconversion. *Chem. Commun.* **60**, 4475–4478 (2024).
6. Ha, D.-G. et al. Exchange controlled triplet fusion in metal–organic frameworks. *Nat. Mater.* **21**, 1275–1281 (2022).
7. Bharmoria, P. et al. Triplet–triplet annihilation based near infrared to visible molecular photon upconversion. *Chem. Soc. Rev.* **49**, 6529–6554 (2020).
8. Naimovičius, L. et al. The statistical probability factor in triplet mediated photon upconversion: a case study with perylene. *J. Mater. Chem. C.* **11**, 14826–14832 (2023).
9. Xu, J. et al. Lanthanide nanoparticles ignite dark molecular triplets. *Sci. China Chem.* **64**, 511–512 (2020).
10. Sun, J. et al. Weakened triplet–triplet annihilation of diiodo–bodipy moieties without influence on their intrinsic triplet lifetimes in diiodo–bodipy–functionalized pillar[5]arenes. *J. Phys. Chem. A* **125**, 2344–2355 (2021).
11. Dong, Y. et al. Low blue–hazard white–light emission based on color–tunable triplet–triplet annihilation upconversion. *J. Colloid Interf. Sci.* **677**, 504–512 (2025).
12. Li, L. et al. Luminescence ratiometric nanothermometry regulated by tailoring annihilators of triplet–triplet annihilation upconversion nanomicelles. *Angew. Chem. Int. Ed.* **60**, 26725 (2021).
13. Ju, Z. et al. Cascade lanthanide-triplet energy transfer for nanocrystal–sensitized organic photon upconversion. *Angew. Chem. Int. Ed.* **64**, 2007306 (2025).
14. Shang, Y. et al. Enhancing solar cell efficiency using photon upconversion materials. *Nanomaterials* **5**, 1782–1809 (2015).
15. Liu, Q. et al. A general strategy for biocompatible, high–effective upconversion nanocapsules based on triplet–triplet annihilation. *J. Am. Chem. Soc.* **135**, 5029–5037 (2013).
16. Hill, S. P. et al. Harnessing molecular photon upconversion in a solar cell at sub-solar irradiance: role of the redox mediator. *J. Am. Chem. Soc.* **139**, 10988–10991 (2017).
17. Monguzzi, A. et al. High efficiency up–converting single phase elastomers for photon managing applications. *Adv. Energy Mater.* **3**, 680–686 (2013).
18. Sasaki, Y. et al. Near–infrared optogenetic genome engineering based on photon–upconversion hydrogels. *Angew. Chem. Int. Ed.* **58**, 17827–17833 (2019).
19. Schulze, T. F. et al. Photochemical upconversion: present status and prospects for its application to solar energy conversion. *Energ. Environ. Sci.* **8**, 103–125 (2015).
20. Lissau, J. S. et al. Photon upconversion from chemically bound triplet sensitizers and emitters on mesoporous ZrO2: implications for solar energy conversion. *J. Phys. Chem. C.* **119**, 25792–25806 (2015).
21. Yin, W. et al. Thermally activated upconversion with metal–free sensitizers enabling exceptional anti–stokes shift and anti–counterfeiting application. *ACS Appl. Mater. Interfaces* **13**, 57481–57488 (2021).
22. Wei, L. et al. Triplet–triplet annihilation upconversion in LAPONITE®/PVP nanocomposites: absolute quantum yields of up to 23.8% in the solid state and application to anti–counterfeiting. *Mater. Horiz.* **9**, 3048–3056 (2022).
23. Khnayzer, R. S. et al. Upconversion–powered photoelectrochemistry. *Chem. Commun.* **48**, 209–211 (2012).
24. Xiao, X. et al. Controlling the triplet states and their application in external stimuli-responsive triplet–triplet–annihilation photon upconversion: from the perspective of excited state photochemistry. *Chem. Soc. Rev.* **50**, 9686–9714 (2021).
25. Cho, H. et al. Efficient near–infrared organic light–emitting diodes with emission from spin doublet excitons. *Nat. Photon.* **18**, 905–912 (2024).
26. Zeng, L. et al. Long wavelength near–infrared and red light-driven consecutive photo–induced electron transfer for highly effective photoredox catalysis. *Nat. Commun.* **15**, 7270 (2024).
27. Kashino, T. et al. Design guidelines for rigid epoxy resins with high photon upconversion efficiency: critical role of emitter concentration. *ACS Appl. Mater. Interfaces* **14**, 22771–22780 (2022).
28. Kim, J.-H. et al. High efficiency low–power upconverting soft materials. *Chem. Mater.* **24**, 2250–2252 (2012).
29. Mori, T. et al. Enhanced upconversion emission in air using novel stretched poly(vinyl alcohol) thin films. *Mol. Syst. Des. Eng.* **3**, 908–916 (2018).
30. Sanders, S. N. et al. Triplet fusion upconversion nanocapsules for volumetric 3D printing. *Nature* **604**, 474–478 (2022).
31. Ye, C. et al. Eco–friendly solid–state upconversion hydrogel with thermoresponsive feature as the temperature indicator. *J. Phys. Chem. C.* **121**, 20158–20164 (2017).
32. Islangulov, R. R. et al. Noncoherent low–power upconversion in solid polymer films. *J. Am. Chem. Soc.* **129**, 12652–12653 (2007).
33. Singh-Rachford, T. N. et al. Influence of temperature on low–power upconversion in rubbery polymer blends. *J. Am. Chem. Soc.* **131**, 12007–12014 (2009).
34. Monguzzi, A. et al. Multicomponent polymeric film for red to green low power sensitized up–conversion. *J. Phys. Chem. A* **113**, 1171–1174 (2009).
35. Wu, W. et al. Organic triplet sensitizer library derived from a single chromophore (BODIPY) with long–lived triplet excited state for triplet–triplet annihilation based upconversion. *J. Org. Chem.* **76**, 7056–7064 (2011).
36. Keivanidis, P. E. et al. Up–conversion photoluminescence in polyfluorene doped with metal(II)–octaethyl porphyrins. *Adv. Mater.* **15**, 2095–2098 (2003).
37. Kang, J.-H. et al. Low-threshold photon upconversion capsules obtained byphotoinduced interfacial polymerization*. *Angew. Chem. Int. Ed.* **51**, 11841–11844 (2012).
38. Duan, P. F. et al. Photon Upconversion in Supramolecular Gel Matrices: Spontaneous Accumulation of Light-Harvesting Donor-

Acceptor Arrays in Nanofibers and Acquired Air Stability. *J. Am. Chem. Soc.* **137**, 1887–1894 (2015).
39. Li, L. et al. Structural color boosted electrochromic devices: strategies and applications. *Adv. Funct. Mater.* **34**, 2311845 (2024).
40. Choi, J. et al. Direct–ink–written cholesteric liquid crystal elastomer with programmable mechanochromic response. *Adv. Funct. Mater.* **34**, 2310658 (2023).
41. Kim, S.-U. et al. Broadband and pixelated camouflage in inflating chiral nematic liquid crystalline elastomers. *Nat. Mater.* **21**, 41–46 (2021).
42. Liu, S. J. et al. Bi–chiral nanostructures featuring dynamic optical rotatory dispersion for polychromatic light multiplexing. *Adv. Mater.* **35**, 2301714 (2023).
43. Ma, J. et al. Mechanochromic, shape–programmable and self–healable cholesteric liquid crystal elastomers enabled by dynamic covalent boronic ester bonds. *Angew. Chem. Int. Ed.* **61**, e202116219 (2022).
44. Schlafmann, K. R. et al. Retention and deformation of the blue phases in liquid crystalline elastomers. *Nat. Commun.* **12**, 4916 (2021).
45. Zhang, P. et al. Pigmented structural color actuators fueled by near-infrared light. *ACS Appl. Mater. Interfaces* **14**, 20093–20100 (2022).
46. Hu, H. et al. Multiple degrees of freedom photoprogramming of soft helical microstructures featuring copper–gated photoswitch. *Matter* **6**, 3927–3939 (2023).
47. Shi, Y. et al. Recyclable soft photonic crystal film with overall improved circularly polarized luminescence. *Nat. Commun.* **14**, 6123 (2023).
48. Xu, M. et al. Exploring the circular polarization capacity from chiral cellulose nanocrystal films for a photo-controlled chiral helix of supramolecular polymers. *Angew. Chem. Int. Ed.* **61**, e202117042 (2022).
49. Feng, Z. et al. Dynamic multimodal information encryption combining programmable structural coloration and switchable circularly polarized luminescence. *Nat. Commun.* **16**, 2264 (2025).
50. Xie, Y. et al. Inverse design of chiral functional films by a robotic AI–guided system. *Nat. Commun.* **14**, 6177 (2023).
51. Yang, X. et al. Electric–Field–regulated energy transfer in chiral liquid crystals for enhancing upconverted circularly polarized luminescence through steering the photonic bandgap. *Adv. Mater.* **32**, 2000820 (2020).
52. Yang, X. et al. Dual band-edge enhancing overall performance of upconverted near-infrared circularly polarized luminescence for anticounterfeiting. *ACS Nano* **17**, 2661–2668 (2023).
53. Chen, Y. et al. Stretchable blue phase liquid crystal lasers with optical stability based on small–strain nonlinear 3D asymmetric deformation. *Adv. Mater.* **37**, 2416448 (2025).
54. Fan, Q. et al. Tunable circular polarization room temperature phosphorescence with ultrahigh dissymmetric factor by cholesteric liquid crystal elastomers. *Cell Rep. Phys. Sci.* **4**, 101583 (2023).
55. Li, S. et al. When quantum dots meet blue phase liquid crystal elastomers: visualized full–color and mechanically–switchable circularly polarized luminescence. *Light Sci. Appl.* **13**, 2047–7538 (2024).
56. Song, Z. P. et al. Mechanically–tunable and full–color circularly polarized long–lived phosphorescence in chiral superstructure elastomers. *Adv. Mater*. 37, 2419640, (2025).
57. Zhang, X. et al. Mechanically tunable circularly polarized luminescence of liquid crystal–templated chiral perovskite quantum dots. *Angew. Chem. Int. Ed.* **63**, e202404202 (2024).
58. Xu, D. et al. Circularly polarized room temperature phosphorescence of chiral bromoxanthone using a chiral self–assembled liquid crystal polymer frameworks. *Adv. Opt. Mater.* **12**, 2303019 (2024).
59. Li, Q. et al. Circularly polarized ultraviolet light–activated asymmetric photopolymerization for the synthesis of CPL–active materials. *Angew. Chem. Int. Ed.* **64**, e202503197 (2025).
60. Luo, J. et al. Ultrastrong circularly polarized luminescence triggered by the synergistic effect of chiral coassembly and selective reflective cholesteric liquid crystal film. *ACS Mater. Lett.* **6**, 2957–2963 (2024).
61. Dzebo, D. et al. Robust triplet–triplet annihilation photon upconversion by efficient oxygen scavenging†. *Photochem. Photobiol. Sci.* **16**, 1327–1334 (2017).
62. Yu, X. et al. Instant locking of molecular ordering in liquid crystal elastomers by oxygen-mediated thiol–acrylate click reactions. *Angew. Chem. Int. Ed.* **130**, 5767–5770 (2018).
63. Hu, Y. et al. Structural model for oxygen permeability of a liquid crystalline polymer. *Macromolecules* **36**, 3606–3615 (2003).
64. Noda, S. et al. Spontaneous-emission control by photonic crystals and nanocavities. *Nat. Photon.* **1**, 449–458 (2007).
65. Liu, Y. et al. Quantum electrodynamics near a photonic bandgap. *Nat. Phys.* **13**, 48–52 (2017).
66. Jia, S. Z. et al. optically ambidextrous reflection circularly polarized luminescence film with high dissymmetry factor and on-demand handedness. *Adv. Optical Mater.* **12**, 2401744 (2024).
67. Kunnummal, A. et al. Upconverted chiral emission in hybrid photonic nanomaterials: toward amplified circularly polarized luminescence with tunable chirality. *ACS Appl. Opt. Mater.* **2**, 2451–2458 (2024).
68. Duan, C. et al. Chiral photonic liquid crystal films derived from cellulose nanocrystals. *Small* **17**, 2007306 (2021).

Acknowledgements

This work was supported by the National Key Basic R&D Research Program of Ministry of Science and Technology of the People's Republic of China (2021YFA1200303, P.D.); the National Natural Science Foundation of China (22205045, T.Z.; 22272109, Z.Y.; 52173159, P.D.; and 92256304, P.D.); the China Postdoctoral Science Foundation (2024M762118, Z.L.); Innovation Research Foundation of Shenzhen (Nos. JCYJ20220818095807016, Z.Y.). We also acknowledge the support from Instrumental Analysis Center of Shenzhen University (Lihu Campus).

Author contributions

P.D., T.Z., and Z.Y. conceived the idea and supervised the project. Z.L., T.Z., Z.Y., and P.D. designed the experiments. Z.L. designed, synthesized, and characterized the materials. Z.L. and H.J. performed the chiroptical study. Z.L., T.Z., J.S., X.J., Z.Y., and P.D. participated in data analysis. Z.L., Z.Y., T.Z., and P.D. wrote and revised the manuscript. All authors analysed and discussed the results and have given approval for the final version of the manuscript.

Competing interests

The authors declare no competing interests.

Additional information

Supplementary information The online version contains supplementary material available at https://doi.org/10.1038/s41467-025-64953-3.

Correspondence and requests for materials should be addressed to Zhen-Qiang Yu, Pengfei Duan or Tonghan Zhao.

Peer review information *Nature Communications* thanks the anonymous reviewers for their contribution to the peer review of this work. A peer review file is available.

Reprints and permissions information is available at http://www.nature.com/reprints

Publisher's note Springer Nature remains neutral with regard to jurisdictional claims in published maps and institutional affiliations.

Open Access This article is licensed under a Creative Commons Attribution-NonCommercial-NoDerivatives 4.0 International License, which permits any non-commercial use, sharing, distribution and reproduction in any medium or format, as long as you give appropriate credit to the original author(s) and the source, provide a link to the Creative Commons licence, and indicate if you modified the licensed material. You do not have permission under this licence to share adapted material derived from this article or parts of it. The images or other third party material in this article are included in the article's Creative Commons licence, unless indicated otherwise in a credit line to the material. If material is not included in the article's Creative Commons licence and your intended use is not permitted by statutory regulation or exceeds the permitted use, you will need to obtain permission directly from the copyright holder. To view a copy of this licence, visit http://creativecommons.org/licenses/by-nc-nd/4.0/.

© The Author(s) 2025